Ultra-stiff amyloid-fibril network of α-synuclein formed by surface seeding reaction confirmed by multichannel electrodeless quartz-crystal-microbalance biosensor

Lianjie Zhou,[†] Touko Hajiri,[†] Kichitaro Nakajima,[†] César Aguirre,[‡] Kensuke Ikenaka,[‡] Hideki Mochizuki,[‡] Keiichi Yamaguchi,[†] Yuji Goto,[†] and Hirotsugu Ogi[*,†]

[†]*Graduate School of Engineering, Osaka University, Yamadaoka 2-1, Suita, 565-0871, Osaka, Japan*

[‡]*Department of Neurology, Graduate School of Medicine, Osaka University, Yamadaoka 2-2, Suita, 565-0871, Osaka, Japan*

E-mail: ogi@prec.eng.osaka-u.ac.jp

Phone: +81-6-6879-7276. Fax: +81-6-6879-7276

Abstract

We develop a multichannel wireless quartz-crystal-microbalance (QCM) biosensor for mechanically studying on-surface aggregation reaction of α-synuclein (α-syn). We find quite unusual change in the resonant frequency that eventually exceeds the baseline, which has never been observed during seeding aggregation reaction. By incorporating growth-to-percolation theory for fibril elongation reaction, we have favorably reproduced this unusual response and found that it can be explained only with formation of ultra-stiff fibril network. We also find that the stiffness of fibril network grown from artificially prepared twist-type seeds is significantly higher than that from rod-type

seeds. Furthermore, the stiffnesses of fibril networks grown from seeds derived from brain tissues of Parkinson's disease (PD) and multiple system atrophy (MSA) patients show very similar trend to those of rod and twist seeds, respectively, indicating that fibrils from MSA patient is stiffer than that from PD.

Keywords

α-Synuclein, Multichannel QCM, Wireless, Fibril Network, Stiffness, Percolation

α-synuclein (α-syn) is an intrinsically disordered protein with 140 amino acids, which takes a monomeric form under normal physiological conditions.[1] Upon fibrillization, α-syn adopts a cross-β structure and stacks into fibrils with β-strands oriented perpendicular to the fibril axis.[2–4] The amyloid fibrils thus formed are the pathological hallmark of neurodegenerative diseases, including PD and MSA.[5–8] Cryo-electron-microscopy studies have revealed the existence of polymorphs in the protofilament structure of α-syn, where the different amino acid sequences involved in the kernel structure and the packing of β-strands result in the formation of fibrils with different twist pitch.[9–12] In addition, it is found that the conformational strains of α-syn fibrils derived from brain tissues or cerebrospinal fluid (CSF) of PD and MSA patients exhibit different morphologies, cytotoxicity, and binding affinity to cell membrane.[13–15] These findings suggest that the different conformations account for the onset of different types of diseases, but the underlying mechanisms have not been fully clarified.[16]

A growing number of studies have shown that the interaction of α-syn with biological membranes plays an important role in the toxicity of α-syn and the development of neurodegenerative diseases.[17–19] It has been reported that aggregates of α-syn formed on surface lead to the disintegration of lipid bilayers,[20,21] formation of tubular structures,[22] and thinning and curvature generation of synaptic vesicles membrane.[23] α-syn also inhibits the fusion of small unilamellar vesicles by changing their surface tension and rigidity.[24] Relatedly, an-

other study shows that growth of α-syn amyloid fibrils on the surface of giant unilamellar vesicles stiffens the membrane and makes the spherical membrane become polyhedral, resulting in extraction of lipids and loss of the vesicle contents.[25] On the other hand, studies on aggregation reactions of amyloidogenic proteins have predominantly used thioflavin T (ThT), a dye specifically bound to the amyloid fibrils, to detect amyloid-fibril formation in bulk solutions.[26,27] However, it has been pointed out that the ThT fluorescence fails to simply reflect the amount of aggregates.[14] Furthermore, the binding of ThT modifies the intrinsic aggregation kinetics and the resultant structure of α-syn aggregates.[28,29] Therefore, a label-free method that detects the on-surface aggregation reaction and the mechanical-property change in the aggregation process will contribute to a better understanding of the neurotoxicity mechanism of α-syn.

In this work, we originally develop a multichannel wireless QCM system to study the α-syn fibrillization behavior on the QCM surface. The seeds of α-syn fibrils are immobilized on the QCM surface, which adsorb the α-syn monomers in the flowing solution and induce the fibril-growth reaction. Importantly, we find very unusual QCM response during the fibril elongation reaction in this study: Because QCM is a mass-sensitive biosensor, it is expected that its resonant frequency would decrease during the fibril-elongation reaction because of deposition of monomers. However, after an initial decrease, the resonant frequency surprisingly increases, even exceeding the baseline. A similar frequency response was reported in a previous study during deposition of glucagon monomers and their aggregations with a low-frequency QCM (5 MHz).[30] However, it was not for the seeding reaction, and the formed protein layer was evaluated to be very soft, being inconsistent with very high stiffness of amyloid fibrils.[31] Such unique frequency response in the surface seeding aggregation of α-syn has never been observed. We have successfully reproduced the experiments by using the fibril growth-to-percolation theory for the multilayer viscoelastic resonator model and find that this unusual frequency response can be only explained by the formation of a highly stiff amyloid-fibril network. Our analysis also reveals that the stiffness of the fibril network

depends on the morphology of the seeds initially immobilized; the more twisted the fibrils, the stiffer the formed network. Furthermore, we perform the measurements using seeds derived from brain tissues of PD and MSA patients. The observed results are consistent with those for the artificial seeds, showing a stiffer fibril network grown from the seeds of MSA patient than that from the PD patient. We attribute such high stiffness of the fibril network to the strong interaction at the cross-over points among fibrils. The findings in this paper thus provide important insights into the effect of α-syn fibrils with different structures on the synucleinopathies and show the potential application of the developed system in the diagnosis of neurodegenerative diseases.

EXPERIMENTAL SECTION

Multichannel Wireless QCM

The sensor cell made of nylon has four pairs of plate antennas (2 mm wide and 1 mm thick) embedded on its top and bottom parts (Fig. S1). The AT-cut quartz resonator has an in-plane size of 2.5×1.7 mm^2 and a thickness of 26 μm. The quartz resonators are lightly sandwiched by the two pieces of silicone rubber at their corners.

Although the impedance analysis has been widely used for measuring the frequency response of a QCM, we adopt the tone-burst excitation instead because the excitation of a wireless QCM requires relatively larger power ($>\sim$10 W). The frequency measurement is performed using our laboratory-built system: A pair of rod-shape antennas serves to generate and detect the shear vibration of the QCM between them in a contactless manner. Each quartz resonator is excited by driving one of the antennas with tone bursts with a duration time of 20 μs through the electromagnetic wave. After the excitation, the resonator continues to oscillate for a while, which can be detected by the other antenna through the electromagnetic wave generated by the oscillating resonator. The amplitude and phase of the driving-frequency component in the received signal are extracted by performing the Fourier

transform, which are used as the outputs. We first measured the resonance spectrum of each QCM by sweeping the driving frequency and measuring the amplitude, giving the resonant frequency. In the real-time monitoring of α-syn aggregation reaction, each resonator is excited using the driving tone bursts of the determined resonance frequency, and the phase change is monitored. The frequency change can be calculated based on the linear phase-frequency relationship near the resonance.[32] By means of a laboratory-built fast switching device, this measurement was performed on each of the four channels in turn. The frequency accuracy (or stability) during the aggregation reaction is about ± 1 ppm/hour, although this value significantly depends on the solution used.

Seed Preparation

To prepare the artificial α-syn seeds, the human wild-type full-length α-syn monomer was first dissolved in Tris-HCl buffer (50 mM, pH7.4) and filtered through a syringe filter with 0.2 μm pore size (Millex-SLGVR04NL). The Tris-HCl buffer with NaCl concentration of 50 mM and 400 mM were used to prepare the twist-type and rod-type fibrils, respectively. The protein concentration was then measured using a spectrophotometer with the extinction coefficient $\epsilon_{1\%}$=3.54 at 280 nm (Thermo Scientific, NanoDrop Lite) and adjusted to 0.5 mg·mL^{-1}. Subsequently, the monomer solution was incubated at 37 °C under ultrasonication. The ultrasonication was performed at 30 kHz for 10 hours in cycles of 1 min irradiation and 9 min quiescence. Next, the incubated solution was centrifugated, and the remaining monomers and oligomers in the supernatant were removed. Finally, we perform continuous ultrasonication to the fibril solution for 1 hour to break the fibrils into short fragments. The fibril concentration was measured by sodium dodecyl sulfate-polyacrylamide gel electrophoresis (SDS-PAGE) as follows: i) Sample solutions after fibril formation were ultracentrifuged for 1 hour at 100,000x g and 25 °C; ii) The supernatant was recovered, and the pellet was resuspended by 50 mM Tris-HCl buffer (pH 7.4); iii) Each fraction was incubated in a urea solution with the final concentration of 6 M overnight at 25 °C under

800-rpm shaking; iv) The sample solutions were boiled for 10 min with the loading buffer (50 mM Tris-HCl pH 6.8, 4% SDS, 2% β-mercaptoethanol, 12% glycerol, and 0.01% bromophenol blue) for SDS-PAGE; v) The SDS-PAGE was performed, and the concentration of each fraction was quantified using a standard curve; and vi) The concentration of fibrils was validated using the concentration of the supernatant. The concentration of obtained twist seeds and rod seeds were 4.93 mg·mL^{-1} and 4.11 mg·mL^{-1}, respectively.

To prepare the seeds from the patients, the protein-misfolding-cyclic-amplification (PMCA) method was adopted as previously described.[33,34] In brief, the amygdala brain homogenates from patients of PD or MSA were added to 0.5 mg·mL^{-1} α-syn monomer solution in Tris-HCl buffer (50 mM, pH7.4, 150 mM NaCl). The mixture was placed in a 96-well plate with 200 μL solution in each well containing 10 μM ThT and was then subjected to cyclic sonication (0.3 seconds irradiation followed by 0.5 seconds pause) at 37 °C. The ThT fluorescence intensity was monitored during the amplification. The derived fibrils were stored at room temperature (25 °C) and fragmented into seeds by sonication directly before use. As demonstrated in Fig. S2, these artificial seeds and seeds from the patients show the ability to form amyloid fibrils quickly.

Transmission Electron Microscopy (TEM) Observation

The morphology observation of obtained seeds was performed on a Hitachi H-7650 transmission electron microscope (Hitachi, Tokyo). The 10-fold diluted sample in deionized water was adsorbed onto copper grids (400-mesh), followed by negative staining with 1% phosphotungstic acid (PTA), and then washed with deionized water. The images were recorded with magnification from 5,000 to 30,000.

Seed Immobilization on QCM Surface

The AT-cut quartz resonators were first cleaned with a piranha solution (98% H_2SO_4:30% H_2O_2 =7:3) and rinsed using ultrapure water. The four resonators were sandwiched by the

thin silicone rubber sheets. To immobilize the seeds on the individual QCMs, 4 μL of the seed solution (Tris-HCl buffer) was dropped on each QCM. For preparing the reference channel, 4 μL of the bovine serum albumin (BSA) solution was dropped. The silicone rubber together with the resonators was then transferred into a culture dish. To keep the seed solution from drying out, we put a layer of buffer-soaked filter paper on the dish bottom and sealed the dish using sealing film (Parafilm). After immobilization at room temperature for 10 hours, we removed the seed solution on the QCM using filter paper and rinsed them using the Tris-HCl buffer. We then dropped 4 μL of 10 mg·mL^{-1} BSA in Tris-HCl buffer on each QCM and incubated for 1 hour at room temperature to block the uncovered areas. Finally, we rinsed the QCMs using the Tris-HCl buffer and packed them in the sensor cell.

Monitoring on-Surface Aggregation Reactions

The sensor cell and the monomer solution were set in a water bath to keep their temperature at 37 °C. The antennas were connected to the switching instrument, and the resonant frequencies of the QCMs were monitored. The Tris-HCl buffer (50 mM, pH7.4) with NaCl concentration of 50 mM or 500 mM was first flowed using a micropump at a flow rate of 800 μL·min^{-1}. The 0.3 mg·mL^{-1} α-syn monomer in the Tris-HCl buffer with NaCl concentration of 50 mM or 500 mM was then flowed to the sensor cell.

Atomic Force Microscopy (AFM) Observation

To observe the fibril morphology on the QCM surface at different elongation stages, the flow of the monomer solution was stopped at an intended time and the QCMs were washed by flowing ultrapure water for 2 min. They were then taken out from the sensor cell and dried in air. The AFM observation of each QCM surface was performed on a scanning probe microscope (Shimadzu, SPM-9600) in ambient conditions. The scanning was performed on several random positions.

Growth-to-Percolation Calculation

Our calculation follows the analysis developed by Åström et al.[35] In the growth-to-percolation calculation, the fibrils are represented by elastic elements with Young's modulus E, Poisson's ratio ν, and width w. Upon cross-linking, the network is considered as a collection of fibril fragments, which are randomly distributed, allowing the assumption that the fragment length follows the Poisson distribution. When the fibril number density and connectivity are uniform in the network layer, its effective stiffness is equivalent to that of the unit fibril layer with thickness w (Fig. S3). The network in this unit layer is constructed by N fibrils per unit area with length $L_f(t)$. The dimensionless fibril density is defined as $q{=}NL_f^2(t)$. Previous studies reveal that the geometric percolation threshold for thin random fibrils occurs at $q{=}5.71$,[36–38] beyond which the fibrils interact with each other because of overlapping. In our calculation, this corresponds to the average fibril length of 0.76 μm as will be shown in the following Results section. For an elastic segment, its rigidity against shear, stretching, and bending deformations vary with its length. Therefore, the segments are considered only to deform in the lowest energy-cost way. The total elastic energy in the network is the summation of the strain energy of each segment associated with shear, stretching, and bending deformations. When the network is treated as a homogeneous plate with the same dimensions having the same strain energy, the effective in-plane Young's modulus $E_e(t)$ and shear modulus $G_e(t)$ are given by[35]

$$E_e(t) = \frac{Ewq}{8L_f(t)} \left\{ \left[3 + \frac{1}{2(1+\nu)} \right] \cdot \left[1 - e^{-z}(1+z) \right] + \left(\frac{2aqw}{\pi L_f(t)} \right)^2 \cdot E_1(z) \right\} \tag{1}$$

$$G_e(t) = \frac{E_e(t)}{2(1+\nu)} \tag{2}$$

where a indicates the fraction of crossing points that are rigidly bonded, $z = \frac{2aql_c}{\pi L_f(t)}$, and $E_1(z) = \int_1^\infty \frac{e^{-zx}}{x} dx$. $l_c = w\sqrt{2(1+\nu)}$ represents the critical length.

In our calculations, we used a constant value for the fibril number density, $N{=}10\ \mu m^{-2}$.

The fibrils were assumed to have a width of w=20 nm[9,16,39] and Poisson ratio ν=0.5. Young's modulus was set as E=0.1∼0.3 GPa, which is within the reported value.[31]

Three-Layer Model Simulation

In the simulation, the parameters describing the properties of the quartz layer and the solution layer are known. The used values were as follows: h_q=26 μm, ρ_q=2654 kg·m^{-3}, μ_q=29 GPa, h_s=3 μm, ρ_s=1000 kg·m^{-3} and η_s=1 mPa·s. For the protein layer, the density was set as ρ_p=1050 kg·m^{-3} considering the close value to that of the solution and its insignificant influence on frequency response.[40]

RESULTS

Multichannel Wireless QCM System

Figures 1 and S1 show the multichannel wireless QCM system originally developed in this study for probing the on-surface aggregation reaction of α-syn. In the sensor cell shown in Fig. S1, we set four AT-cut quartz resonators, which are lightly fixed at their one corner by sandwiching them with two pieces of silicone rubber. We drop 4 μL seed solutions to immobilize the seeds on the resonator surfaces (Fig. 1A). After washing the surfaces with the buffer solution, we set the silicone rubber sheets in the sensor cell to form the fluidic channel for flowing the α-syn monomer solution. We use antennas that are embedded in the upper and bottom parts of the sensor cell to excite and detect their shear vibrations. Importantly, in this wireless manner, we can avoid depositing metallic films on the resonator surfaces as electrodes, thereby being able to use extremely thin quartz resonators and improve the sensitivity of the QCM.[41] The QCM used in this study has a thickness of 26 μm and a theoretical through-thickness shear-wave resonance frequency near 64.5 MHz in air. The measured spectra in Fig. S4 show a lower resonance frequency near 64.37 MHz (although slight variation can be observed due to the subtle thickness difference of the fabricated quartz

resonators), which is expected because of the seed immobilization and in-liquid measurement, indicating a good frequency accuracy of our system.

The resonance-frequency changes of these resonators are monitored with the originally developed system as explained in the experimental section. All the measurements were performed at 37 °C. A micropump is used to flow the monomer solution. Using this system, we can monitor the resonant frequencies of the four QCMs independently without interference between channels even their resonance frequencies are almost the same as demonstrated in Fig. S4. Very importantly, since all the quartz resonators are exposed to the same solution, the aggregation reaction from different seeds can be simultaneously studied under the same condition, which has not been achieved previously. The resonators in the flowing solution are illustrated in Fig. 1B. We thus immobilized different α-syn seeds on each QCM surface and flow the α-syn monomer solution. In some experiments, we immobilized BSA instead of seeds as the control channel. Figure 1C shows a typical measurement result, where resonant frequencies were simultaneously measured when different materials were immobilized on the four resonators. As shown in Fig. S2, we confirmed that the seeds used in this study show the ability to accelerate the fibril-formation reaction in bulk solutions.

There is *in principle* the possibility of cross-contamination between different resonators since the same solution flows over all the resonator surfaces. We therefore ensured sufficient lateral spacing between QCMs of about six times the QCM width. The AFM images on the QCM surfaces shown later confirm that no fibril transport between channels occurs during the fibril on-surface elongation reaction.

Monitoring of the α-Syn on-Surface Seeding Reaction

Depending on solution conditions as well as the seed, α-syn fibrils formed from the same monomers have different morphologies.[16,39,42] We prepared α-syn fibrils with two distinct morphologies (rod and twist types) and broke them into fibril fragments by sonication.[33] Figure 2A shows their TEM images. The rod seeds predominantly have two parallel protofil-

aments, while the twist seeds comprise two intertwined protofilaments. These morphologies are consistent with those reported.[2,31,33] Both types of seeds have an equivalent average length of around 50 nm. From Fig. 2B, we can clearly see the formation of the fibril network composed of dense fibrils on the QCM surfaces, on which these seeds were immobilized, by flowing the monomer solution. However, few fibrils can be observed on the reference QCM, where BSA covered the resonator surfaces at the beginning. Unlike fibrillization in a bulk solution, because the seeds were separately immobilized on the QCM surface, the cross-linking between the fibrils occurs when fibrils grow to a certain length. As the growth progresses, the fibril network is eventually formed over the QCM surface.

Figure 2C shows the frequency responses of QCMs during the flow of the monomer solution. Because of the absence of seed, the frequency of the control channel shows a slight decrease, which can be attributed to the non-specific adsorption of α-syn monomers on BSA. However, in the QCMs on which the seeds were initially immobilized, the frequency first decreases to a minimum and then significantly increases. It is surprising that the frequency even exceeds the baseline. In the conventional biosensor application of QCM, the binding of target molecules on the QCM surface increases the effective mass of the resonator and then decreases the resonant frequency, as supported by Sauerbrey's equation.[43] In the case of the formation of a viscoelastic protein layer, the viscoelastic property change also affects the resonant frequency, especially that of a high frequency QCM.[44,45] As pointed out in our previous study,[46] a low-frequency QCM (for example, 5 MHz) extends the acoustic shear field from its surface up to $\sim$250 nm, beyond the thickness of a thin protein layer ($<\sim$100 nm), leading to relatively low sensitivity to the viscoelasticity of thin protein layer. The higher frequency QCM used in this study confines the shear field within $\sim$70 nm from the surface, which contributes to a better sensitivity to the viscoelasticity. As can be confirmed from the AFM images, the early stage of elongation results in the increase in the fibril mass at the QCM surface, which contributes to the frequency decrease. On the other hand, the viscoelastic properties of the α-syn fibril layer are expected to change significantly with fibril

cross-linking, resulting in a significant increase in the frequency. Although the frequency responses for QCMs with rod and twist seeds show similar trends, the differences in the amount of frequency variation indicate that the fibril network layers originated from the two different seeds have different mechanical properties.

Viscoelasticity of α-Syn Fibril-Network Layer

From the AFM images in Fig. 2B, we consider that the α-syn seeding reaction proceeds on QCM surface as illustrated in Fig. 3A. The seed fragments are initially immobilized on the QCM surface with random position and orientation. As the fibril length increases, the fibrils reach the percolation threshold,[36] where the cross-linking and connection between fibrils occur. (In this paper, percolation refers to the progress in the connectivity in a randomly distributed fibril system, which is different from the process of a liquid moving slowly through a porous medium. The percolation threshold here is defined as the point at which long-range connectivity of fibrils is formed in the fibril system.) Subsequently, the fibril network forms on the QCM surface. We consider that the evolution of the mechanical properties of such disordered fibril networks is identical to the systems such as fibrous materials,[47] carbon-nanotube mats,[48] and extracellular matrix:[49,50] The effective stiffness of these network systems depends not only on the elastic property of the constituent fibrils but also more sensitively on the cross-linking connectivity after the percolation threshold.[51,52] We here propose a model for explaining the unusual frequency response using this growth-to-percolation model.

In our measurement, the QCM extends the acoustic shear field to the adjacent α-syn fibril layer, in turn, the property change in the fibril layer affects its frequency response. The resonant frequency of QCM with the α-syn fibril layer attached to its surface in monomer solution can be calculated using the three-layer model.[40,53] As illustrated in Fig. 3B, the three-layer model consists of the elastic quartz resonator, the viscoelastic protein layer (α-syn fibril layer), and the Newtonian solution layer. With the stress-free boundary condition

at the QCM bottom surface and solution top surface, and the continuous condition of the shear stress and particle velocity at each interface, the frequency change of QCM is given by[45,54]

$$\Delta f \approx \frac{1}{2\pi\rho_q h_q}\mathrm{Im}\left(\kappa_p\xi_p\frac{1-Ae^{2\xi_p h_p}}{1+Ae^{2\xi_p h_p}}\right) \tag{3}$$

where $A=\frac{\kappa_p\xi_p+\eta_s\xi_s\tanh(\xi_s h_s)}{\kappa_p\xi_p-\eta_s\xi_s\tanh(\xi_s h_s)}$, $\kappa_p=\frac{\mu_p^*}{j\omega}$, $\xi_p=\sqrt{-\frac{\rho_p\omega^2}{\mu_p^*}}$, $\xi_s=\sqrt{\frac{j\rho_s\omega}{\eta_s}}$, $\mu_p^*=\mu_p+j\omega\eta_p$. Here, ρ, h, η, μ, and ω denote mass density, thickness, viscosity, shear modulus, and angular frequency. The subscripts q, p, and s represent quantities of quartz, protein, and solution, respectively.

We systematically investigated the influences of the four key parameters (thickness, mass density, viscosity, and stiffness) of the protein layer on the resonant frequency and find that only the stiffness change can cause this unusual increase in the resonant frequency as shown in Fig. S5. Therefore, we focus on the evolution of the effective stiffness of the protein layer and simulate it using the growth-to-percolation model.[35,47]

We first assumed a sigmoidal change for the average fibril length[55] shown as the green curve in Fig. 3C and calculated the effective stiffness as described in the experimental section. To evaluate the influence of the property of the constituent fibril on the network stiffness, we investigated three possible cases: (i) The single-fibril Young's modulus E equals 0.244 GPa, and the network connectivity a, which represents the fraction of the number of the rigidly bound crossover points, is 0.6; (ii) E=0.149 GPa and a=0.6; and (iii) E=0.149 GPa and a=0.2. As shown in Fig. 3C, at the early elongation stage before the percolation threshold, which is defined in the experimental section, the protein layer has very low stiffness because the fibrils are not connected. Beyond the percolation threshold, the network stiffness rapidly increases with the increase of the fibril length. As expected, an increase in Young's modulus or the rigid crossover point stiffens the fibril network. The stiffness of the formed network can be as high as ∼900 kPa when the α-syn fibrils elongate to 2.5 μm, which is much higher compared with that of muscle tissue (∼12 kPa)[56] and dermal tissue (0.5-2 kPa).[57]

We also assumed sigmoidal changes for the thickness and viscosity of the protein layer as

shown in Figs. 3D and 3E and fixed the mass density to be constant (1.05 g·cm^{-3}) because of its less sensitivity to the frequency change (Fig. S5A). We then obtain the simulation results in good agreement with the QCM measurements as shown in Fig. 3F. Although there are adjustable parameters for calculating the final frequency change (maximum value and half-time value for each sigmoid function, for example), the critical parameter is the stiffness of the fibril-network layer as demonstrated in Fig. S5. It is important to note that we fail to reproduce the experimental result without the significant stiffness evolution as shown in Fig. 3C.

While the stiffness shows a delayed and relatively slow increase at the early stage, it is needed that the thickness and viscosity immediately increase without showing a lag time (Figs. 3D and 3E) to reproduce the experiments. Therefore, the early-stage frequency decrease mainly originates from the mass accumulation. However, after the fibril length reaches the percolation threshold, the effective stiffness of the protein layer significantly increases with the cross-linking among fibrils, leading to the increase in the QCM frequency. The minimum point on the frequency curve thus indicates the moment when the stiffness increase overwhelms the mass-loading effect. Here, we refer to this time as the cross-linking initiation time (CLIT). The consistency between the simulated frequency responses and the measurement results suggests that the fibrils grown from the twist seeds are stiffer than those from the rod seeds by a factor of about two. It should be noted that when the fibril network has less network connectivity, as in the third case in Fig. 3C, the frequency fails to show a significant increase after CLIT even if the single fibril shows a sufficiently large Young's modulus. This behavior explains the measurements for the aggregation reaction of amyloid β peptides on QCM[45] (Fig. S6). Because the effective stiffness of the fibril network is highly affected by the inter-fibril connectivity as shown in Fig. S7, the drastic frequency increase after CLIT, which is observed in α-syn fibrils, indicates the strong inter-fibril connectivity between α-syn fibrils.

Fibril Morphology Determines the Network Stiffness

To further investigate the relationship between the fibril morphology and the network stiffness, we monitored the α-syn aggregation reaction using the wireless QCM at a higher NaCl concentration of 500 mM. At this salt concentration, elongated fibrils show different morphologies due to the conformation change of α-syn monomer as has been reported in our recent study,[33] which is also confirmed in bulk solutions as shown in Fig. S2: In the early stage of the seeding reaction, there is no remarkable difference in the seeding reaction between with rod and twist seeds at the low NaCl concentration (Fig. S2A), but the seeding reaction with rod seeds proceeds faster than that with twist seeds at the high NaCl concentration (Fig. S2B).

Figure 4A shows the measurement results of the α-syn seeding reaction when the monomer solution containing 500 mM NaCl was flowed and the corresponding fibril networks on the QCM surfaces. The dashed lines in the frequency responses are simulation results with the evolution of the fibril-network stiffness shown in Fig. 4B. (The corresponding thickness and viscosity changes are shown in Fig. S8A.) As can be seen from the AFM images, both the number and length of the fibril after 3 h are larger than those grown at a lower salt concentration as shown in Fig. 2B, indicating that the elongation reaction is accelerated at higher NaCl concentration. This acceleration behavior by increasing the salt concentration is also found in the bulk experiment (Fig. S2), especially for the rod seeds. Correspondingly, CLIT at 500 mM NaCl comes earlier than that at 50 mM NaCl for both rod and twist seeds (Fig. 4C). The AFM images in Fig. 4D summarize the morphologies of the fibrils elongated from the rod and twist seeds at different salt concentrations. By comparing the twist periodicity and Young's modulus of the single fibril, we note that the more twisted the constituent fibrils, the stiffer the fibril and thus the stiffer the formed network. Previous AFM studies of α-syn fibrils indicate that the twist period may affect the fibril rigidity, suggesting that fibrils with shorter twist periods exhibit higher stiffness.[31]

α-Syn on-Surface Seeding Reaction from Seeds Derived from PD and MSA Patients

We derived α-syn fibrils from the brain homogenates of patients with PD and MSA by the PMCA method.[33] The obtained fibril seeds after ultrasonic fragmentation are shown in Fig. 5A. The dominant morphology of the MSA seeds is twist type, and the seeds from PD are mainly composed of rod-type seeds. (The twist-type seeds also appear, but their twist period is longer ($>\sim$100 nm).) Figure 5B shows the measured frequency responses (solid lines) and simulated results (broken lines) for the on-surface seeding reactions using the patient seeds. The frequency responses with the seeds from PD and MSA are very similar to those with rod-type and twist-type artificial seeds, respectively, indicating nearly the same percolation and network formation processes during the fibril elongation reaction as can be confirmed from the AFM images (Fig. 5B). The estimated change in the effective stiffness of the fibril network is shown in Fig. 5C. (Corresponding thickness and viscosity changes are shown in Fig. S8B.) The results indicate the higher stiffness of the fibril network grown from the MSA seeds than from the PD seeds. From the AFM images (Fig. 5D), we analyzed the twist periodicity of the resultant fibrils. The fibrils from PD and MSA patients exhibit an average periodicity of 71.7 nm and 56.9 nm, respectively (Fig. 5E). The correlation between the twist period and the fibril stiffness is again indicated.

DISCUSSION AND CONCLUSIONS

Multichannel QCM is highly promising in bioassay because it enables the detection of multiple targets in a single measurement, leading to a substantial reduction in cost, sample volume, and diagnostic time. At present, two main types of multichannel QCMs have been reported. The first type (one-chip multichannel QCM) consists of a single quartz plate, the surface of which is divided into several regions with separate electrodes.[58–60] In this configuration, the acoustic and electric interferences become the serious issue, and this type of sensor

failed to be used as a biosensor. The second type is a combination of several independent QCMs.[61] The separation of fluidic channels in this type imposes restrictions on measuring complex reactions in the same solution. Although we previously developed a multichannel wireless QCM with several quartz resonators set in one fluidic channel,[62,63] all the channels were driven by the same antenna. Consequently, quartz plates with different thicknesses and frequencies must be used, leading to sensitivity discrepancy in different channels. Also, the inter-channel interference remained unsolved. The multichannel QCM developed in this work operates wirelessly by independent antennas in each channel. Therefore, α-syn aggregation reactions with different seeds can be studied using identical QCMs under the same solution condition without the inter-channel interference.

Not only the electrical interference between the channels but also interference of biochemical reactions between channels can be neglected with the current experimental setup as follows. For example, assuming that the $\sim$200 ppm frequency reduction in Fig. 3F would be caused by deposition of α-syn monomers, it corresponds to a deposition of 4 pmol of monomers from the Sauerbrey equation[43] and the QCM area. This value is much smaller than the total number of monomers in the microchannel ($\sim$4 nmol). Furthermore, since the monomers are constantly supplied by the flow system, the adsorption/desorption reactions at each QCM surface have little influence on the reaction conditions of the system.

Combination with the three-layer model and QCM experiment has been an accepted method for evaluating the viscoelastic property of thin protein layers. Because of the simple and homogeneous model, the simulation results cannot completely fit the QCM measurements. However, the essential trend is reproduced: As can be seen in Fig. 3F, 4A, and 5B, our simulated results consistently explain the corresponding measurements, validating the correctness of the simulation results. Because there is no other reliable method for measuring the viscoelastic parameters of protein layers in solution, the multichannel QCM system developed in this work could provide important insights into the physical properties of α-syn on-surface aggregation.

In this study, we show many QCM responses during the on-surface seeding reaction of α-syn, where the resonant frequency significantly increases after the initial drop, even eventually exceeding the baseline (Figs.1C, 2C, 4A, and 5B). As mentioned above, this is an unexpected result because the QCM is a mass-sensitive biosensor, which normally shows frequency decrease because of the deposition of flowing monomers. One therefore may attribute this unusual behavior to the detachment of surface aggregates together with the initially immobilized seeds. However, we can dismiss this possibility for two reasons. First, as shown in Figs. 2B, 4A, and 5B, we confirmed the formation of dense fibril networks on QCM surfaces using AFM. Second, as shown in Fig. S9, the amplitude of the resonant vibration continued to decrease during the aggregation reaction, even with the significant increase of the resonant frequency for the seed-immobilized channel. Because of the increase in the viscoelastic resistance in liquid, the vibrational amplitude is reduced as the viscoelastic layer grows. We fail to observe such a significant decrease in the vibrational amplitude for the BSA channel, on which few monomers are accumulated, supporting the view that the protein layer continues to grow even after the frequency increase.

The AFM observations suggested that the thicknesses of the fibril-network layers formed from the rod and twisted seeds are of similar value (30$\sim$100 nm), and we assumed the same final thickness in the numerical simulation as shown in Fig. 3D for reproducing the experimental frequency changes. However, since the seeding experiments in bulk solutions in Fig. S2 indicate the higher ability of the rod seed in capturing monomers than the twist seed, one may consider that the different QCM response between the rod and twist seeds would be caused by the thinner network layer from the twist seeds than from the rod seeds. However, this should have further increased their discrepancy as demonstrated in Fig. S10, and it is needed that the effective stiffness of the fibril network from twist seeds is significantly higher than that from rod seeds.

We assumed a final thickness of $\sim$100 nm after the on-surface seeding reaction (Fig. 3D), which may seem too large because of the fibril diameter of $\sim$20 nm or less. However, unlike

the thickness evaluated by AFM in a dry condition, the thickness probed by QCM represents an *effective* thickness of the protein layer, in which the dynamic behavior of flexible fibrils and their interaction with monomers in liquid are involved. Therefore, the effective thickness evaluated by QCM is usually larger than the AFM thickness.

α-syn fibrils with different polymorphs have a similar structure of stacked α-syn polypeptide chains. The β-stands held by a densely packed network of hydrogen bonds form the fibril backbone with the unstructured region in the polypeptide chain surrounding the core. Besides the amino residues constituting the core, the stacking structure, including the helical rise and twist angle between each β-stand, varies in different polymorphs, leading to different twist periodicity of the fibrils.[64,65] It has been reported that α-syn fibrils amplified from brain homogenates using the PMCA method have a periodicity of 88 nm from MSA, 107 nm, and 93 nm from PD patients.[66] Another study observed a range from 46 to 105 nm for MSA and 77 to199 nm for PD.[14] The periodicity of the MSA fibrils in this work agrees with those of previous studies, while that of the PD fibrils shows a slightly lower value, possibly due to the on-surface growth. Nonetheless, the MSA fibrils have shown more twisted morphology than the PD fibrils. Considering the low elasticity of neurons around several kilopascals,[67,68] the stiffness of the fibril network up to $\sim$0.9 MPa found here implies that the ultrahigh stiffness of the α-syn aggregates on the cell membrane or the Lewy body[69,70] will be a key for causing corresponding diseases.

In the stiffness analysis, we assumed the same fraction of the rigid cross-linking point (a) both for the fibril networks grown from PD and MSA seeds. From the AFM images, the value of a for the MSA seeds seems to be similar to (or slightly smaller than) that from the PD seeds. Therefore, the higher stiffness of the single MSA fibril is needed in order to explain the experiments. The mechanical strength of a single amyloid fibril stems from the dense hydrogen-bond network with the dominant contribution from the β-stands core.[71–73] The circular-dichroism-spectroscopy analysis performed on fibrils amplified from PD and MSA patients has reported a higher proportion of β-sheet structure in MSA fibrils than that

in PD fibrils.[14] Hence, the higher stiffness of the MSA fibril than the PD fibril can be attributed to the higher proportion of the β-sheet structure. Although the behind mechanism remains to be elucidated, our findings reveal that the α-syn fibril network can show a very high stiffness. This will be caused by the long unstructured residues exposed perpendicularly to the fibril axis. For an α-syn fibril, relatively less ordered flexible regions extend from fibril's lateral face, and it is significantly longer ($\sim$40 residues plus a shorter N-terminus).[74] These unstructured regions may interact with each other to construct the rigid inter-fibril connection. Also importantly, the developed multichannel wireless QCM system provides a label-free monitoring of the on-surface aggregation reaction and the mechanical property change, demonstrating the potential application in the diagnosis of neurodegenerative diseases.

Finally, the most important advantage of the system we have developed in this study is the ability to monitor different aggregation reactions from different seeds under the same solution conditions. Using this unique system, for example, by immobilizing different antibody on each channel, it will be possible to study in detail the time-series changes of various aggregates and their transitions to different species during the protein aggregation process in the same solution.

ASSOCIATED CONTENT

Supporting Information

Configuration of multichannel QCM biosensor, bulk seeding thioflavin-T assay, fibril network layer, resonance spectra measured by multichannel QCM, numerical study of sensitivity of protein-layer parameters on QCM frequency response, surface seeding reaction for amyloid β, network stiffness with various crossover bond ratio, thickness and viscosity changes during formation of α-syn network layer, amplitude responses of QCM, additional comparison between simulation and experiment (PDF)

AUTHOR INFORMATION

Corresponding Authors

*E-mail ogi@prec.eng.osaka-u.ac.jp (H.O.).

Author Contributions

L.Z. performed the QCM measurements, analyzed data, and wrote the paper. T.H. performed the QCM experiments. K.N. performed the seeding assay in bulk solutions. C.A., K.I., and H.M. prepared and evaluated the seeds, took the TEM images, and contributed discussions. K.Y. and Y.G. prepared the monomers and contributed discussions. H.O. (corresponding author) promoted this study, developed the multichannel QCM system, analyzed the results, and wrote the paper.

ACKNOWLEDGMENTS

This research was partially supported by JSPS KAKENHI Grant (No. 19H00862) and Development of Advanced Measurement and Analysis Systems from Japan Science and Technology Agency (No. JP-MJSN16B5).

References

(1) Jakes, R.; Spillantini, M. G.; Goedert, M. Identification of two distinct synucleins from human brain. *FEBS Letters* **1994**, *345*, 27–32.

(2) Vilar, M.; Chou, H. T.; Lührs, T.; Maji, S. K.; Riek-Loher, D.; Verel, R.; Manning, G.; Stahlberg, H.; Riek, R. The fold of α-synuclein fibrils. *Proc. Natl. Acad. Sci. U.S.A.* **2008**, *105*, 8637–8642.

(3) Giasson, B. I.; Murray, I. V.; Trojanowski, J. Q.; Lee, V. M. A Hydrophobic Stretch of 12 Amino Acid Residues in the Middle of α-Synuclein Is Essential for Filament Assembly. *J. Biol. Chem.* **2001**, *276*, 2380–2386.

(4) Serpell, L. C.; Berriman, J.; Jakes, R.; Goedert, M.; Crowther, R. A. Fiber diffraction of synthetic α-synuclein filaments shows amyloid-like cross-β conformation. *Proc. Natl. Acad. Sci. U.S.A.* **2000**, *97*, 4897–4902.

(5) Polymeropoulos, M. H.; Lavedan, C.; Leroy, E.; Ide, S. E.; Dehejia, A.; Dutra, A.; Pike, B.; Root, H.; Rubenstein, J.; Boyer, R. et al. Mutation in the α-synuclein gene identified in families with Parkinson's disease. *Science* **1997**, *276*, 2045–2047.

(6) Spillantini, M. G.; Schmidt, M. L.; Lee, V. M.; Trojanowski, J. Q.; Jakes, R.; Goedert, M. α-synuclein in Lewy bodies. *Nature* **1997**, *388*, 839–840.

(7) Tu, P. H.; Galvin, J. E.; Baba, M.; Giasson, B.; Tomita, T.; Leight, S.; Nakajo, S.; Iwatsubo, T.; Trojanowski, J. Q.; Lee, V. M. Glial cytoplasmic inclusions in white matter oligodendrocytes of multiple system atrophy brains contain insoluble α-synuclein. *Ann. Neurol.* **1998**, *44*, 415–422.

(8) Spillantini, M. G.; Crowther, R. A.; Jakes, R.; Cairns, N. J.; Lantos, P. L.; Goedert, M. Filamentous α-synuclein inclusions link multiple system atrophy with Parkinson's disease and dementia with Lewy bodies. *Neurosci. Lett.* **1998**, *251*, 205–208.

(9) Li, B.; Ge, P.; Murray, K. A.; Sheth, P.; Zhang, M.; Nair, G.; Sawaya, M. R.; Shin, W. S.; Boyer, D. R.; Ye, S. et al. Cryo-EM of full-length α-synuclein reveals fibril polymorphs with a common structural kernel. *Nat. Commun.* **2018**, *9*, 3609.

(10) Guerrero-Ferreira, R.; Taylor, N. M.; Mona, D.; Ringler, P.; Lauer, M. E.; Riek, R.; Britschgi, M.; Stahlberg, H. Cryo-EM structure of alpha-synuclein fibrils. *eLife* **2018**, *7*, e36402.

(11) Schweighauser, M.; Shi, Y.; Tarutani, A.; Kametani, F.; Murzin, A. G.; Ghetti, B.; Matsubara, T.; Tomita, T.; Ando, T.; Hasegawa, K. et al. Structures of α-synuclein filaments from multiple system atrophy. *Nature* **2020**, *585*, 464–469.

(12) Kumar, S. T.; Mahul-Mellier, A.-L.; Hegde, R. N.; Rivière, G.; Moons, R.; de Opakua, A. I.; Magalhães, P.; Rostami, I.; Donzelli, S.; Sobott, F. et al. A NAC domain mutation (E83Q) unlocks the pathogenicity of human alpha-synuclein and recapitulates its pathological diversity. *Sci. Adv.* **2022**, *8*, eabn0044.

(13) Strohäker, T.; Jung, B. C.; Liou, S. H.; Fernandez, C. O.; Riedel, D.; Becker, S.; Halliday, G. M.; Bennati, M.; Kim, W. S.; Lee, S. J. et al. Structural heterogeneity of α-synuclein fibrils amplified from patient brain extracts. *Nat. Commun.* **2019**, *10*, 5535.

(14) Shahnawaz, M.; Mukherjee, A.; Pritzkow, S.; Mendez, N.; Rabadia, P.; Liu, X.; Hu, B.; Schmeichel, A.; Singer, W.; Wu, G. et al. Discriminating α-synuclein strains in Parkinson's disease and multiple system atrophy. *Nature* **2020**, *578*, 273–277.

(15) Prusiner, S. B.; Woerman, A. L.; Mordes, D. A.; Watts, J. C.; Rampersaud, R.; Berry, D. B.; Patel, S.; Oehler, A.; Lowe, J. K.; Kravitz, S. N. et al. Evidence for α-synuclein prions causing multiple system atrophy in humans with parkinsonism. *Proc. Natl. Acad. Sci. U.S.A.* **2015**, *112*, E5308–E5317.

(16) Bousset, L.; Pieri, L.; Ruiz-Arlandis, G.; Gath, J.; Jensen, P. H.; Habenstein, B.; Madiona, K.; Olieric, V.; Böckmann, A.; Meier, B. H. et al. Structural and functional characterization of two alpha-synuclein strains. *Nat. Commun.* **2013**, *4*, 2575.

(17) Cooper, A. A.; Gitler, A. D.; Cashikar, A.; Haynes, C. M.; Hill, K. J.; Bhullar, B.; Liu, K.; Xu, K.; Strathearn, K. E.; Liu, F. et al. α-synuclein blocks ER-Golgi traffic and Rab1 rescues neuron loss in Parkinson's models. *Science* **2006**, *313*, 324–328.

(18) Kamp, F.; Exner, N.; Lutz, A. K.; Wender, N.; Hegermann, J.; Brunner, B.; Nuscher, B.; Bartels, T.; Giese, A.; Beyer, K. et al. Inhibition of mitochondrial fusion by α-synuclein is rescued by PINK1, Parkin and DJ-1. *EMBO J.* **2010**, *29*, 3571–3589.

(19) Auluck, P. K.; Caraveo, G.; Lindquist, S. α-synuclein: Membrane interactions and toxicity in Parkinson's disease. *Annu. Rev. Cell Dev. Biol.* **2010**, *26*, 211–233.

(20) Reynolds, N. P.; Soragni, A.; Rabe, M.; Verdes, D.; Liverani, E.; Handschin, S.; Riek, R.; Seeger, S. Mechanism of membrane interaction and disruption by α-synuclein. *J. Am. Chem. Soc.* **2011**, *133*, 19366–19375.

(21) Zhu, M.; Li, J.; Fink, A. L. The association of α-synuclein with membranes affects bilayer structure, stability, and fibril formation. *J. Biol. Chem.* **2003**, *278*, 40186–40197.

(22) Jiang, Z.; Messieres, M. D.; Lee, J. C. Membrane remodeling by α-synuclein and effects on amyloid formation. *J. Am. Chem. Soc.* **2013**, *135*, 15970–15973.

(23) Braun, A. R.; Sevcsik, E.; Chin, P.; Rhoades, E.; Tristram-Nagle, S.; Sachs, J. N. α-synuclein induces both positive mean curvature and negative gaussian curvature in membranes. *J. Am. Chem. Soc.* **2012**, *134*, 2613–2620.

(24) Braun, A. R.; Sachs, J. N. α-synuclein reduces tension and increases undulations in simulations of small unilamellar vesicles. *Biophys. J.* **2015**, *108*, 1848–1851.

(25) Chaudhary, H.; Subramaniam, V.; Claessens, M. M. Direct Visualization of Model Membrane Remodeling by α-Synuclein Fibrillization. *ChemPhysChem* **2017**, *18*, 1620–1626.

(26) Naiki, H.; Higuchi, K.; Hosokawa, M.; Takeda, T. Fluorometric determination of amyloid fibrils in vitro using the fluorescent dye, thioflavine T. *Anal. Biochem.* **1989**, *177*, 244–249.

(27) Biancalana, M.; Koide, S. Molecular mechanism of Thioflavin-T binding to amyloid fibrils. *Biochim. Biophys. Acta* **2010**, *1804*, 1405–1412.

(28) D'Amico, M.; Carlo, M. G. D.; Groenning, M.; Militello, V.; Vetri, V.; Leone, M. Thioflavin T promotes Aβ(1-40) amyloid fibrils formation. *J. Phys. Chem. Lett.* **2012**, *3*, 1596–1601.

(29) Kumar, H.; Singh, J.; Kumari, P.; Udgaonkar, J. B. Modulation of the extent of structural heterogeneity in α-synuclein fibrils by the small molecule thioflavin T. *J. Biol. Chem.* **2017**, *292*, 16891–16903.

(30) Hovgaard, M. B.; Dong, M.; Otzen, D. E.; Besenbacher, F. Quartz crystal microbalance studies of multilayer glucagon fibrillation at the solid-liquid interface. *Biophys. J.* **2007**, *93*, 2162–2169.

(31) Makky, A.; Bousset, L.; Polesel-Maris, J.; Melki, R. Nanomechanical properties of distinct fibrillar polymorphs of the protein α-synuclein. *Sci. Rep.* **2016**, *6*, 37970.

(32) Ogi, H.; Fukunishi, Y.; Omori, T.; Hatanaka, K.; Hirao, M.; Nishiyama, M. Effects of flow rate on sensitivity and affinity in flow injection biosensor systems studied by 55-MHz wireless quartz crystal microbalance. *Anal. Chem.* **2008**, *80*, 5494–5500.

(33) Aguirre, C.; Ikenaka, K.; So, M.; Maruno, T.; Yamaguchi, K.; Nakajima, K.; Choong, C.-J.; Nabekura, K.; Beck, G.; Tomii, K. et al. Conformational change in the monomeric alpha-synuclein imparts fibril polymorphs. *bioRxiv* **2022**, DOI: 10.1101/2022.02.10.479831.

(34) Shahnawaz, M.; Tokuda, T.; Waraga, M.; Mendez, N.; Ishii, R.; Trenkwalder, C.; Mollenhauer, B.; Soto, C. Development of a biochemical diagnosis of Parkinson disease by detection of α-synuclein misfolded aggregates in cerebrospinal fluid. *JAMA Neurol.* **2017**, *74*, 163–172.

(35) Åström, J. A.; Mäkinen, J. P.; Hirvonen, H.; Timonen, J. Stiffness of compressed fiber mats. *J. Appl. Phys.* **2000**, *88*, 5056–5061.

(36) Pike, G. E.; Seager, C. H. Percolation and conductivity: A computer study. I. *Phys. Rev. B* **1974**, *10*, 1421–1434.

(37) Niskanen, K. J.; Alava, M. J. Planar random networks with flexible fibers. *Phys. Rev. Lett.* **1994**, *73*, 3475–3478.

(38) Wilhelm, J.; Frey, E. Elasticity of stiff polymer networks. *Phys. Rev. Lett.* **2003**, *91*, 108103.

(39) Sidhu, A.; Segers-Nolten, I.; Subramaniam, V. Solution conditions define morphological homogeneity of α-synuclein fibrils. *Biochim. Biophys. Acta* **2014**, *1844*, 2127–2134.

(40) Shagawa, T.; Torii, H.; Kato, F.; Ogi, H.; Hirao, M. Viscoelasticity evolution in protein layers during binding reactions evaluated using high-frequency wireless and electrodeless quartz crystal microbalance biosensor without dissipation. *Jpn. J. Appl. Phys.* **2015**, *54*, 096601.

(41) Ogi, H. Wireless-electrodeless quartz-crystal-microbalance biosensors for studying interactions among biomolecules: A review. *Proc. Jpn. Acad., Ser. B* **2013**, *89*, 401–417.

(42) Hoyer, W.; Antony, T.; Cherny, D.; Heim, G.; Jovin, T. M.; Subramaniam, V. Dependence of α-synuclein aggregate morphology on solution conditions. *J. Mol. Biol.* **2002**, *322*, 383–393.

(43) Sauerbrey, G. The use of quartz oscillators for weighing thin layers and for microweighing. *Z. Phys.* **1959**, *155*, 206–222.

(44) Lucklum, R.; Behling, C.; Hauptmann, P. Role of mass accumulation and viscoelastic film properties for the response of acoustic-wave-based chemical sensors. *Anal. Chem.* **1999**, *71*, 2488–2496.

(45) Lai, Y. T.; Ogi, H.; Noi, K.; Kato, F. Viscoelasticity Response during Fibrillation of Amyloid β Peptides on a Quartz-Crystal-Microbalance Biosensor. *Langmuir* **2018**, *34*, 5474–5479.

(46) Shagawa, T.; Torii, H.; Kato, F.; Ogi, H.; Hirao, M. Relationship between viscosity change and specificity in protein binding reaction studied by high-frequency wireless and electrodeless MEMS biosensor. *Jpn. J. Appl. Phys.* **2015**, *54*, 068001.

(47) Cox, H. L. The elasticity and strength of paper and other fibrous materials. *Br. J. Appl. Phys.* **1952**, *3*, 72–79.

(48) Åström, J. A.; Krasheninnikov, A. V.; Nordlund, K. Carbon nanotube mats and fibers with irradiation-improved mechanical characteristics: A theoretical model. *Phys. Rev. Lett.* **2004**, *93*, 215503.

(49) Beroz, F.; Jawerth, L. M.; Münster, S.; Weitz, D. A.; Broedersz, C. P.; Wingreen, N. S. Physical limits to biomechanical sensing in disordered fibre networks. *Nat. Commun.* **2017**, *8*, 16096.

(50) Sun, B. The mechanics of fibrillar collagen extracellular matrix. *Cell Rep. Phys. Sci.* **2021**, *2*, 100515.

(51) Broedersz, C. P.; Mao, X.; Lubensky, T. C.; Mackintosh, F. C. Criticality and isostaticity in fibre networks. *Nat. Phys.* **2011**, *7*, 983–988.

(52) Head, D. A.; MacKintosh, F. C.; Levine, A. J. Nonuniversality of elastic exponents in random bond-bending networks. *Phys. Rev. E* **2003**, *68*, 025101.

(53) Reed, C. E.; Kanazawa, K. K.; Kaufman, J. H. Physical description of a viscoelastically loaded AT-cut quartz resonator. *J. Appl. Phys.* **1990**, *68*, 1993–2001.

(54) Voinova, M. V.; Rodahl, M.; Jonson, M.; Kasemo, B. Viscoelastic Acoustic Response

of Layered Polymer Films at Fluid-Solid Interfaces: Continuum Mechanics Approach. *Phys. Scr.* **1999**, *59*, 391–396.

(55) Nakajima, K.; Toda, H.; Yamaguchi, K.; So, M.; Ikenaka, K.; Mochizuki, H.; Goto, Y.; Ogi, H. Half-Time Heat Map Reveals Ultrasonic Effects on Morphology and Kinetics of Amyloidogenic Aggregation Reaction. *ACS Chem. Neurosci.* **2021**, 3456–3466.

(56) Engler, A. J.; Griffin, M. A.; Sen, S.; Bönnemann, C. G.; Sweeney, H. L.; Discher, D. E. Myotubes differentiate optimally on substrates with tissue-like stiffness: Pathological implications for soft or stiff microenvironments. *J. Cell Biol.* **2004**, *166*, 877–887.

(57) Achterberg, V. F.; Buscemi, L.; Diekmann, H.; Smith-Clerc, J.; Schwengler, H.; Meister, J. J.; Wenck, H.; Gallinat, S.; Hinz, B. The nano-scale mechanical properties of the extracellular matrix regulate dermal fibroblast function. *J. Invest. Dermatol.* **2014**, *134*, 1862–1872.

(58) Tatsuma, T.; Watanabe, Y.; Oyama, N.; Kitakizaki, K.; Haba, M. Multichannel quartz crystal microbalance. *Anal. Chem.* **1999**, *71*, 3632–3636.

(59) Tao, W.; Lin, P.; Ai, Y.; Wang, H.; Ke, S.; Zeng, X. Multichannel quartz crystal microbalance array: Fabrication, evaluation, application in biomarker detection. *Anal. Biochem.* **2016**, *494*, 85–92.

(60) Jin, X.; Huang, Y.; Mason, A.; Zeng, X. Multichannel Monolithic Quartz Crystal Microbalance Gas Sensor Array. *Anal. Chem.* **2009**, *81*, 595–603.

(61) Amer, M. A.; Turo, A.; Salazar, J.; Berlanga-Herrera, L.; Garcia-Hernandez, M. J.; Chavez, J. A. Multichannel QCM-based system for continuous monitoring of bacterial biofilm growth. *IEEE Trans. Instrum. Meas.* **2019**, *69*, 2982–2995.

(62) Ogi, H.; Nagai, H.; Fukunishi, Y.; Yanagida, T.; Hirao, M.; Nishiyama, M. Multichannel

wireless-electrodeless quartz-crystal microbalance immunosensor. *Anal. Chem.* **2010**, *82*, 3957–3962.

(63) Noi, K.; Iijima, M.; Kuroda, S.; Ogi, H. Ultrahigh-sensitive wireless QCM with bio-nanocapsules. *Sens. Actuat. B, Chem.* **2019**, *293*, 59–62.

(64) Sweers, K. K.; Segers-Nolten, I. M.; Bennink, M. L.; Subramaniam, V. Structural model for α-synuclein fibrils derived from high resolution imaging and nanomechanical studies using atomic force microscopy. *Soft Matter* **2012**, *8*, 7215–7222.

(65) Li, Y.; Zhao, C.; Luo, F.; Liu, Z.; Gui, X.; Luo, Z.; Zhang, X.; Li, D.; Liu, C.; Li, X. Amyloid fibril structure of α-synuclein determined by cryo-electron microscopy. *Cell Res.* **2018**, *28*, 897–903.

(66) Burger, D.; Fenyi, A.; Bousset, L.; Stahlberg, H.; Melki, R. Cryo-EM structure of alpha-synuclein fibrils amplified by PMCA from PD and MSA patient brains. *bioRxiv* **2021**, DOI: 10.1101/2021.07.08.451588.

(67) Spedden, E.; White, J. D.; Naumova, E. N.; Kaplan, D. L.; Staii, C. Elasticity maps of living neurons measured by combined fluorescence and atomic force microscopy. *Biophys. J.* **2012**, *103*, 868–877.

(68) Spedden, E.; Staii, C. Neuron biomechanics probed by atomic force microscopy. *Int. J. Mol. Sci.* **2013**, *14*, 16124–16140.

(69) Marotta, N. P.; Ara, J.; Uemura, N.; Lougee, M. G.; Meymand, E. S.; Zhang, B.; Petersson, E. J.; Trojanowski, J. Q.; Lee, V. M. Alpha-synuclein from patient Lewy bodies exhibits distinct pathological activity that can be propagated in vitro. *Acta Neuropathol. Commun.* **2021**, *9*, 188.

(70) Spillantini, M. G.; Crowther, R. A.; Jakes, R.; Hasegawa, M.; Goedert, M. α-Synuclein

in filamentous inclusions of Lewy bodies from Parkinson's disease and dementia with Lewy bodies. *Proc. Natl. Acad. Sci. U.S.A.* **1998**, *95*, 6469–6473.

(71) Knowles, T. P.; Buehler, M. J. Nanomechanics of functional and pathological amyloid materials. *Nat. Nanotechnol.* **2011**, *6*, 469–479.

(72) Knowles, T. P.; Fitzpatrick, A. W.; Meehan, S.; Mott, H. R.; Vendruscolo, M.; Dobson, C. M.; Welland, M. E. Role of intermolecular forces in defining material properties of protein nanofibrils. *Science* **2007**, *318*, 1900–1903.

(73) Ruggeri, F. S.; Adamcik, J.; Jeong, J. S.; Lashuel, H. A.; Mezzenga, R.; Dietler, G. Influence of the β-sheet content on the mechanical properties of aggregates during amyloid fibrillization. *Angew. Chem. Int. Ed.* **2015**, *54*, 2462–2466.

(74) Törnquist, M.; Michaels, T. C.; Sanagavarapu, K.; Yang, X.; Meisl, G.; Cohen, S. I.; Knowles, T. P.; Linse, S. Secondary nucleation in amyloid formation. *Chem. Commun.* **2018**, *54*, 8667–8684.

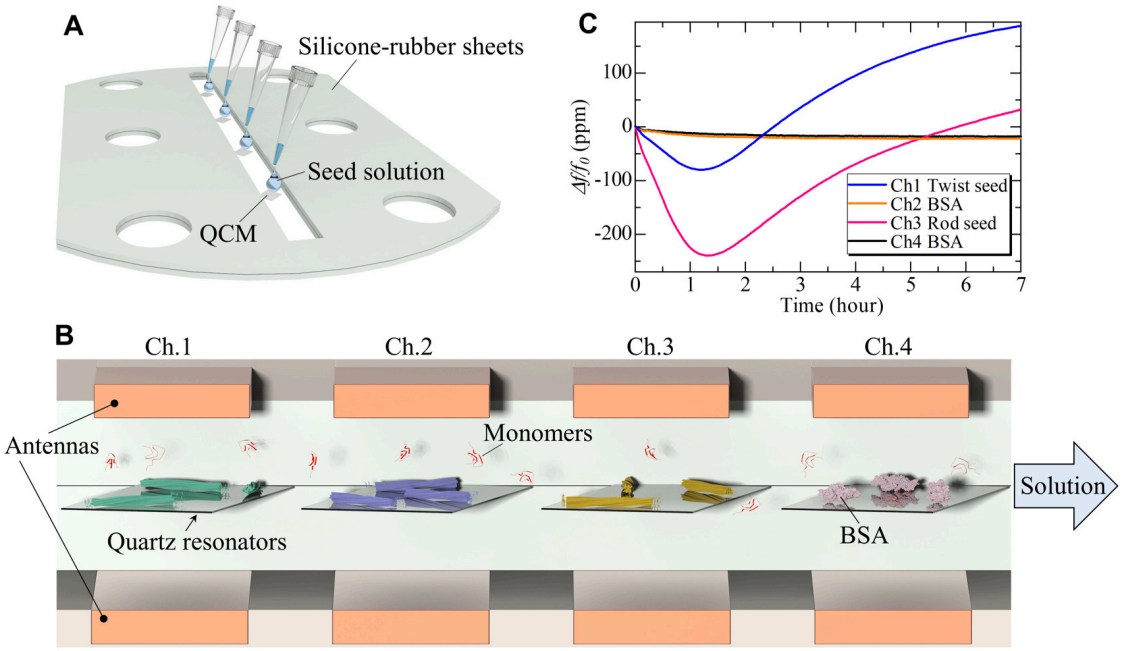

Figure 1: (A) Schematic illustration of the immobilization of α-syn seeds on the resonator surfaces. (B) Illustration inside the sensor cell, where the α-syn aggregation reactions proceed on the different resonators during the monomer-solution flow. Different seeds are immobilized on the different resonator surfaces, and BSA is immobilized on the reference channel. (C) An example of the four-channel QCM experiment during the monomer-solution flow, where different α-syn seeds and BSA are immobilized on different QCMs.

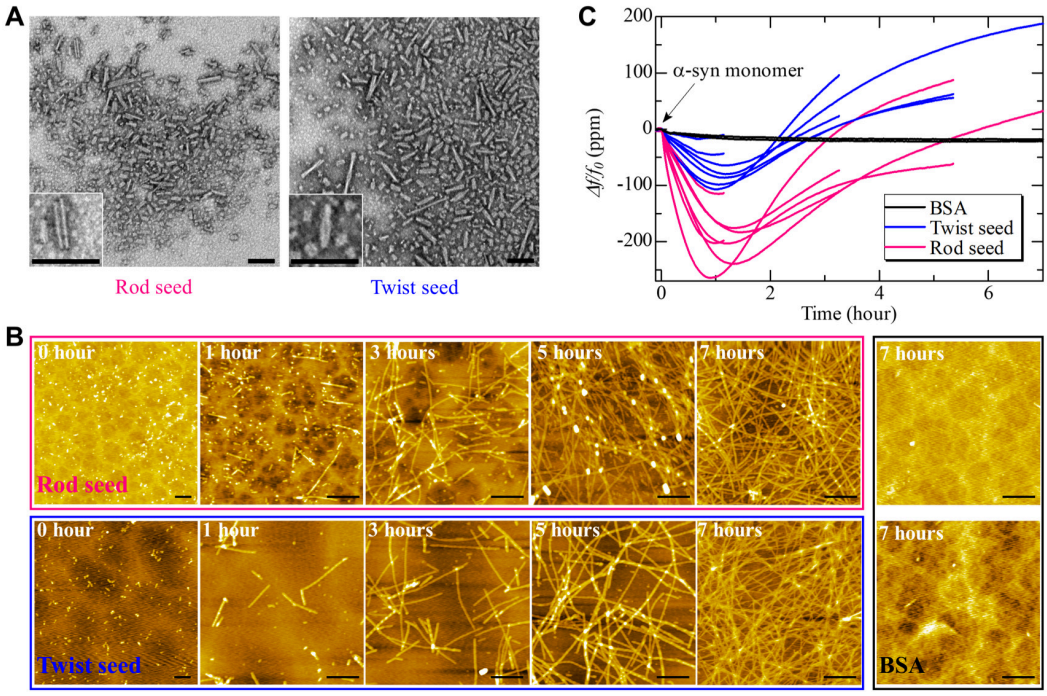

Figure 2: (A) TEM images of seeds with rod structure (left) and twist structure (right). (B) AFM images of the fibrils formed on the QCM surfaces at various times during the fibril elongation reaction with NaCl concentration of 50 mM. (C) Frequency responses of QCMs with rod and twist seeds and that with BSA (without seed) during the α-syn monomer-solution flow with NaCl concentration of 50 mM. Scale bars in (A) and (B) indicate 100 nm and 500 nm, respectively.

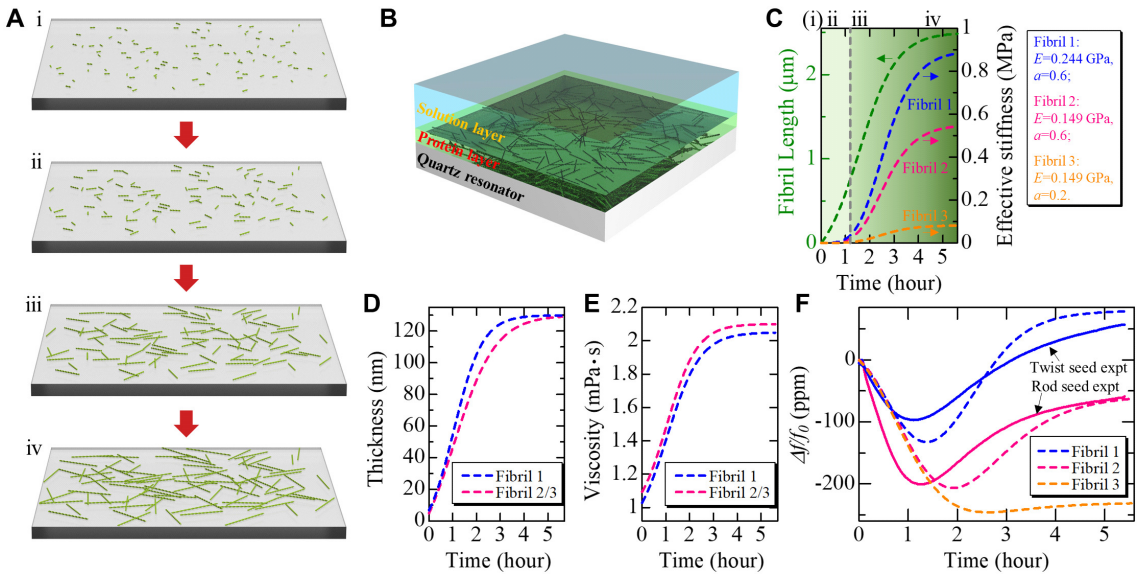

Figure 3: (A) Illustration of the fibril elongation behavior on QCM surface characterized by four stages: (i) The initial stage with randomly immobilized seed fragments; (ii) The fibril-elongation stage before reaching the percolation; (iii) The cross-linking stage, resulting in a sparsely linked network; (iv) The fibril-elongation stage after the percolation along with a rapid increase in the network connectivity. (B) Schematic of the three-layer model. (C) The effective stiffness change of the fibril-network layer as the fibril length increases calculated by the growth-to-percolation model. The percolation threshold is indicated by the gray broken line. The calculation is performed on three types of constituent fibrils with different Young's moduli E and the cross-over bond ratios a at the same fibril number density. (D) Thickness change and (E) viscosity change of the fibril layer used in the three-layer model simulation. (F) Reproduced frequency responses of QCM. The simulation results (dashed lines) are compared with the measurement results (solid lines).

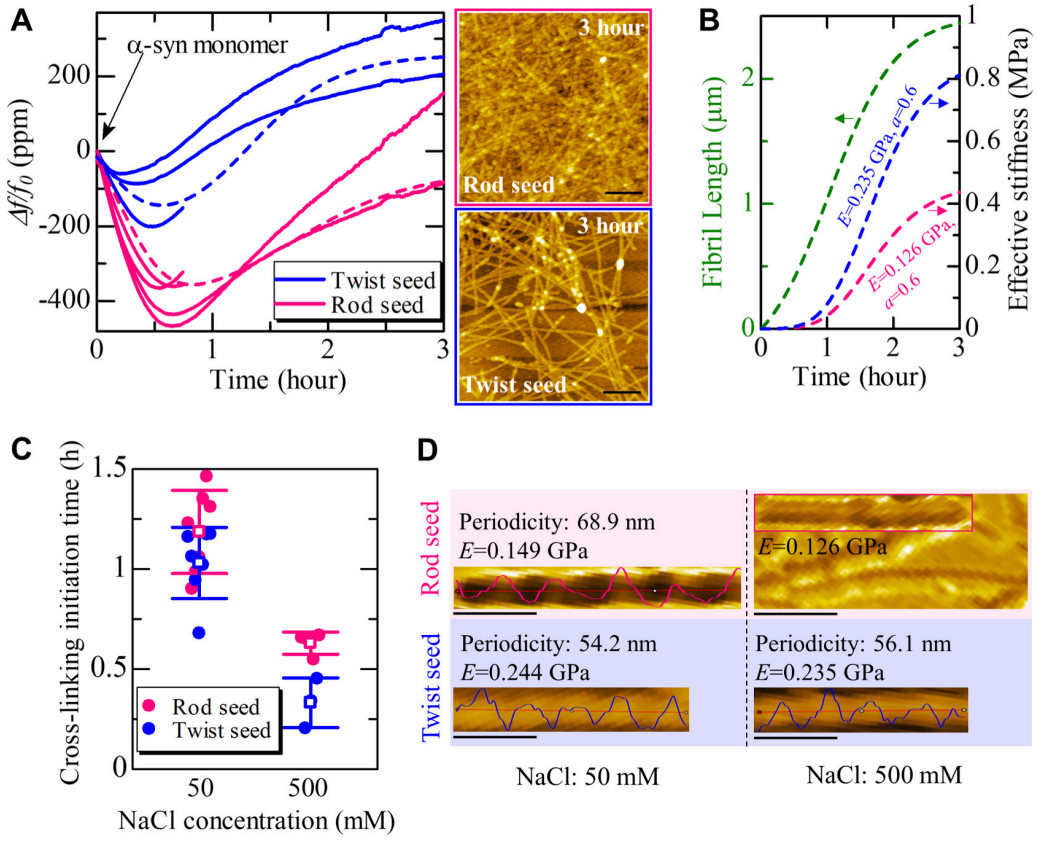

Figure 4: (A) (left) Frequency responses of QCMs with initial seeds on their surfaces during the flow of α-syn monomer solution with NaCl concentration of 500 mM. Dashed lines show the simulation results. (right) AFM images on the QCM surfaces at 3 h. (B) The effective stiffness changes for the fibril network layer calculated by the growth-to-percolation model, which reproduce the experiments in (A). (C) The cross-linking initiation time (CLIT) at different NaCl concentrations. Error bars indicate the standard deviation (n=3). (D) The AFM phase images which show the structure difference of the α-syn fibrils grown from different seeds and in different NaCl concentrations. The twist period and estimated Young's modulus are shown. Scale bars: 500 nm (A) and 100 nm (D).

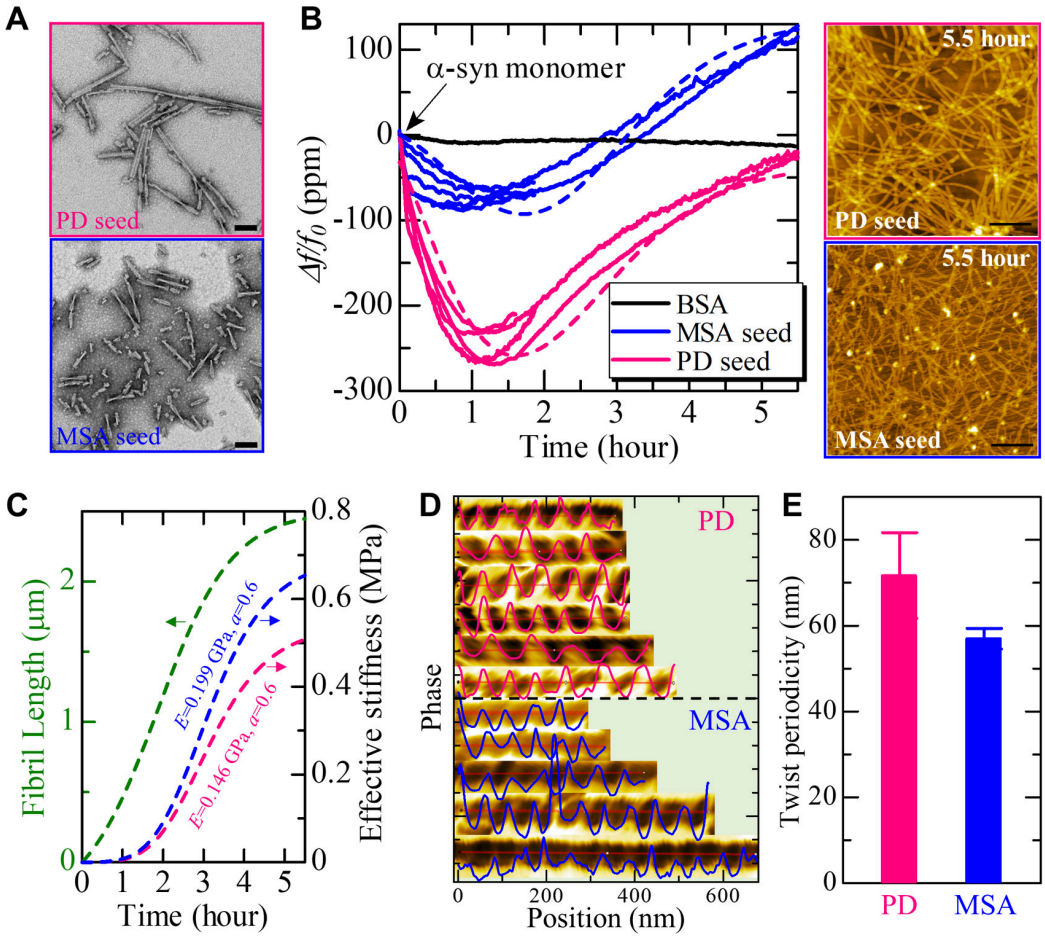

Figure 5: (A) TEM images of seeds amplified from the brain tissue of patients with PD and MSA. (B) (left) Frequency responses of QCMs with initial seeds from PD and MSA on their surfaces during the flow of α-syn monomer solution with NaCl concentration of 50 mM. Dashed lines show the simulation results. (right) AFM images on the QCM surface at 5.5 hours. (C) The effective stiffness changes for the fibril network layer calculated by the growth-to-percolation model, which reproduce the experiments in (B). (D) The structure difference of α-syn fibrils elongated from PD and MSA seeds. (E) The twist periodicity of α-syn fibrils elongated from PD and MSA seeds. Error bars indicate the standard deviation (n=6). Scale bars: 100 nm in (A) and 500 nm in (B).